Highlights

A Quadrilateral Inverse Plate Element for Real-time Shape-sensing and Structural Health Monitoring of Thin Plate Structures

Ihtisham Khalid,Zahid Ahmed Qureshi,Haris Ali Khan,Selda Oterkus,Erkan Oterkus

- Investigation of inverse finite element method using a sub-parametric approach for thin plate structures

- Inverse-plate element formulation based on bi-linear and non-conforming cubic Hermite basis functions

- High numerical accuracy in full-field reconstruction of displacement profiles for thin plate structures subjected to in-plane, out-of-plane, and mixed general loading conditions

- Accurate validation of defect identification and quantification methodology for thin plate structures

- Computational efficiency and superior capability of the proposed inverse-plate element in real-time shape-sensing and Structural Health Monitoring applications for structures, which can be modelled as thin plates

A Quadrilateral Inverse Plate Element for Real-time Shape-sensing and Structural Health Monitoring of Thin Plate Structures

Ihtisham Khalid[a], Zahid Ahmed Qureshi[a,*], Haris Ali Khan[a], Selda Oterkus[b] and Erkan Oterkus[b]

[a]*Department of Aerospace Engineering, College of Aeronautical Engineering, National University of Sciences & Technology, Islamabad, 44000, Pakistan*
[b]*Department of Naval Architecture, Ocean & Marine Engineering, University of Strathclyde, Glasgow, G4 0LZ, Scotland, United Kingdom*

ARTICLE INFO

ABSTRACT

The inverse finite element method (iFEM) emerged as a powerful tool in shape-sensing and structural health monitoring (SHM) applications with distinct advantages over existing methodologies. In this study, a quadrilateral inverse-plate element is formulated via a sub-parametric approach using bilinear and non-conforming cubic Hermite basis functions for engineering structures, which can be modeled as thin plates. Numerical validation involves dense and assumed sparse sensor arrangements for in-plane, out-of-plane, and mixed general loading conditions. iFEM analysis reveals efficient monotonic convergence to analytical and high-fidelity finite element reference solutions. After successful numerical validation, defect detection analysis is performed considering minute geometric discontinuities and structural stiffness reduction because of latent subsurface defects under tensile and transverse loading conditions. The inverse formulation successfully resolves the presence of simulated defects under a sparse sensor arrangement. The proposed inverse-plate element is accurate in the full-field reconstruction of shape-sensing profiles and reliable in defect identification and quantification in thin plate structures.

1. Introduction

Structural analysis is crucial in structural design to ensure the safety and integrity of structures during their entire service life. Engineering structures are designed to undertake the operational and environmental conditions efficiently for their proposed lifespan. Meanwhile, structural maintenance aspects keep evolving and improving with every industrial revolution. Nowadays, Structural Health Monitoring (SHM) systems are considered an integral part of the structural design and analysis process. Engineering structures are analyzed widely using various numerical techniques based on different mathematical approaches, including conventional and mixed finite element methods [1, 2, 3], semi-analytical approaches [4, 5], variational techniques [6], and, more recently, peridynamics [7, 8]. Similarly, data-driven approaches based on Deep Neural Networks (DNN) offer significant benefits in predicting structural behavior through pattern recognition. These techniques [9, 10, 11] can handle both forward and inverse analysis within the same framework and are robust enough to inherently deal with uncertainties. Consequently, they represent valuable alternatives for structural analysis.

Shape-sensing is a practical approach for monitoring structural integrity and, therefore, extensively researched in the literature. Ko et al. developed a shape-sensing strategy for beams and plate structures using Ko's Displacement Theory [12, 13], which relies on the assumptions of Euler

Bernoulli's beam theory to correlate axial strains with the second-order derivative of deflection in plate bending. Various studies showed the application of global and piecewise continuous basis functions to approximate strain fields for full-field reconstruction of displacements [14, 15, 16]. Since these functions can help accurately represent deformation fields, Kirchhoff plate assumptions were employed to define strain displacement fields in plate structures. Modal Methods based on Modal Transformation Theory (MTT) were studied in detail [17, 18] to reconstruct the displacement profiles from normal mode shapes by utilizing appropriate strain displacement relations. Shkarayev et al. [19] apply least squares to reconstruct displacements in a two-step approach, which requires reconstruction of applied loading as a first step, followed by reconstruction of the displacement field. Later, variational approaches governed by suitable error-functional were utilized together with FEM approximations to present pragmatic full-field shape reconstruction capabilities within the framework of the inverse finite element method (iFEM).

In recent years, the iFEM approach has gained much attention in shape-sensing because it aligns well with SHM's general implementation strategy [20]. Sensor systems are used to collect structural data, which is then processed within the framework of iFEM to reach meaningful conclusions about the structure's health and integrity state. The framework of iFEM was initially introduced by Tessler and Spangler [21, 22] for the real-time full-field reconstruction of three-dimensional displacement and stress profiles using instrumented strain data. These reconstructed displacement and stress profiles help to identify the damage's existence, location, and severity. The type and characterization of the damage strictly depend on the failure mode mechanics incorporated in the underlying iFEM formulations and interpretations of results.

Over the last decade, iFEM has been extensively utilized for full-field shape-sensing of engineering structures, including beams, plates, and sandwich panels. Various inverse elements have been proposed and analyzed to implement the iFEM methodology [23, 24, 25]. Tessler and Spangler [26] proposed the first three-node inverse element iMIN3 for the shape-sensing of plate and shell structures for general loading conditions. The element was designed on First Order Shear Deformation Theory (FSDT) mechanics. Kefal et al. [27, 28] proposed a two-dimensional four-node quadrilateral inverse shell element iQS4 and an eight-node curved inverse shell element iCS8 for its application in different marine and offshore structures. To overcome the discretization issues in curved shell structures, isogeometric inverse elements [29, 30] were used for iFEM analysis of these structures under reduced sensor arrangement. A two-node inverse beam element iBeam3 [31] demonstrated the accuracy and robustness in iFEM analysis of beams and similar structures. You et al. [32] successfully employed it to monitor the deformation process of a buried pipe during the freeze-thaw process. de Mooij et al. [33] formulated a twenty-node solid inverse element to extend the application of iFEM in three-dimensional analysis. i3-RZT was developed by Kefal et al. [34, 35] for accurate shape-sensing of multi-layer composite laminates and sandwich panels. Recently, Li et al. [36] proposed a two-dimensional four-node quadrilateral plane stress element iQP4 and analyzed it for various in-plane loading conditions with reduced sensor arrangement.

Most of the reported inverse elements in the literature are Mindlin-based. These elements include transverse shear strain effects, require C^0 continuity across elements, and are applicable to both thick and thin plate structures. However, these elements suffer from shear locking when dealing with thin plate situations because of the excessive influence of the transverse shear deformation terms. Strategies such as selective and reduced integration are often used to mitigate shear locking but can introduce unwanted spurious mechanisms. Kirchhoff plate theory, unlike Mindlin plate theory, neglects transverse shear deformations. This simplification is crucial because it eliminates the need to model and solve for transverse shear strains, which can introduce additional complexity and potential sources of error. Unlike Mindlin-based elements, Kirchhoff-based elements require the deflection field to have C^1 continuity because of the presence of second derivatives of the deflection in the virtual work expression. Ensuring such strict continuity between elements can be difficult and often necessitates the use of non-conforming elements in practical applications.

Within the iFEM framework, these elements have wide applicability in aerospace, marine, and renewable energy sectors for shape sensing and SHM of engineering structures that can be modeled as thin plates. Recent technological advancements have led to a shift in the use of composite structures, transitioning them from secondary to primary structural components. This shift has created a demand for thicker composite structures capable of sustaining heavier

loads. In response to these requirements, sandwich configurations have gained prominence. These configurations offer superior strength-to-weight ratio, higher shear stiffness, and excellent energy absorption capabilities. In most sandwich designs, thin and stiff face sheets are combined with compliant cores, leading to significant differences in stiffness and thickness between the face sheets and the core. To accurately model these differences in an equivalent single layer, it is necessary to simultaneously employ both Mindlin and Kirchhoff plate assumptions. Therefore, developing Kirchhoff inverse elements is crucial for advancing shape-sensing capabilities and effectively undertaking SHM of not only thin plate structures but also allied sandwich configurations.

This study reports the usage of bi-linear and non-conforming cubic Hermite basis functions to formulate a two-dimensional quadrilateral inverse-plate element. The proposed inverse element suits thin plates subjected to in-plane, out-of-plane, and mixed in-plane and out-of-plane loading conditions. Considering the efficiency of real-time shape-sensing in SHM, the inverse element is formulated using a sub-parametric approach where geometric mapping is performed using bi-linear basis functions. A detailed validation study is accomplished for the proposed inverse-plate element under dense and sparse sensor arrangement by considering three numerical cases: plane stress, pure bending, and mixed in-plane and out-of-plane loading conditions. The results obtained for the proposed inverse-plate element have been compared against analytical and high-fidelity FEM results, which serve as the reference solution. For its utilization in SHM applications, the defect resolution capability of the newly proposed elements is analyzed by considering geometric discontinuities and subsurface defects under tensile and transverse loading conditions. Displacement and von Mises contours are analyzed to identify, quantify, and resolve the simulated defects, which usually appear in thin plate structures. Finally, the capability of the newly proposed inverse-plate element is discussed for its application in real-time shape-sensing and SHM applications of thin plate structures.

The rest of the article is organized as follows. The theoretical background and detailed inverse element formulation steps are described in the next section. The numerical validation section provides a standardized iFEM analysis setup and problem statement for three validation cases. The defect analysis section provides a mathematical modeling approach for defects and their prediction using the current iFEM formulation. The explicit forms of bi-linear and non-conforming cubic Hermite basis functions used in inverse-plate element formulation are expressed in the Appendix to replicate research analyses.

2. Formulation of Inverse-Plate Element

Kirchhoff plate theory is widely used for the analysis of thin-walled structures where the thickness of the plate is sufficiently smaller than the characteristic dimension of the plate. It is an extension of the Euler-Bernoulli beam

theory representing two-dimensional plate structures. The displacement field, according to Kirchhoff's assumptions, can be written as:

$$u(x, y, z) = u_o(x, y) - z\frac{\partial w_o(x, y)}{\partial x} \tag{1a}$$

$$v(x, y, z) = v_o(x, y) - z\frac{\partial w_o(x, y)}{\partial y} \tag{1b}$$

$$w(x, y, z) = w_o(x, y) \tag{1c}$$

In these displacement equations, the subscript $_{(o)}$ indicates that the displacements are determined at the mid-plane of the plate at $z = 0$. The displacement field variables u_o and v_o represent in-plane displacements along the longitudinal and lateral axis of the plate, whereas w_o represents out-of-plane deflection. In addition to the transverse deflection, two slopes, $\frac{\partial w_o(x,y)}{\partial x}$ and $\frac{\partial w_o(x,y)}{\partial y}$, represent the bending rotation of the plate section about the y and x axis, respectively.

The strain field for the Kirchhoff plate can now be derived using the displacement field written in equation (1a), (1b), and (1c) by employing the following kinematic relations:

$$\epsilon_{xx} = \frac{\partial u}{\partial x} = \frac{\partial u_o}{\partial x} - z\frac{\partial^2 w_o}{\partial x^2} \tag{2a}$$

$$\epsilon_{yy} = \frac{\partial v}{\partial y} = \frac{\partial v_o}{\partial y} - z\frac{\partial^2 w_o}{\partial y^2} \tag{2b}$$

$$\gamma_{xy} = \frac{\partial u}{\partial y} + \frac{\partial v}{\partial x} = \frac{\partial u_o}{\partial y} + \frac{\partial v_o}{\partial x} - 2z\frac{\partial^2 w_o}{\partial x\partial y} \tag{2c}$$

The strain field of Kirchhoff plate theory consists of two in-plane normal strains ϵ_{xx}, ϵ_{yy}, and an in-plane shear strain γ_{xy} only. Transverse strains $\epsilon_{zz} = \gamma_{yz} = \gamma_{xz} = 0$ vanish because of Kirchhoff's kinematic assumptions in defining the thin plate structures.

The strain field can be rewritten more conveniently by segregating the membrane and bending curvatures separately in the equation as (2a), (2b), and (2c).

$$\epsilon(u) = \epsilon^o(u) + \kappa(u) \tag{3}$$

$$\epsilon(u) = \begin{Bmatrix} \epsilon_{xx} \\ \epsilon_{yy} \\ \gamma_{xy} \end{Bmatrix} = \begin{Bmatrix} \epsilon^o_{xx} \\ \epsilon^o_{yy} \\ \gamma^o_{xy} \end{Bmatrix} + z\begin{Bmatrix} \kappa_{xx} \\ \kappa_{yy} \\ \kappa_{xy} \end{Bmatrix} \tag{4}$$

where, $\epsilon^o(u)$ represents the membrane strains:

$$\epsilon^o(u) = \begin{Bmatrix} \epsilon^o_{xx} \\ \epsilon^o_{yy} \\ \gamma^o_{xy} \end{Bmatrix} = \begin{Bmatrix} \dfrac{\partial u_o}{\partial x} \\ \dfrac{\partial v_o}{\partial y} \\ \dfrac{\partial u_o}{\partial y} + \dfrac{\partial v_o}{\partial x} \end{Bmatrix} \tag{5}$$

and $\kappa(u)$ represents the bending strains associated with bending curvatures.

$$\kappa(u) = \begin{Bmatrix} \kappa_{xx} \\ \kappa_{yy} \\ \kappa_{xy} \end{Bmatrix} = \begin{Bmatrix} -\dfrac{\partial^2 w_o}{\partial x^2} \\ -\dfrac{\partial^2 w_o}{\partial y^2} \\ -2\dfrac{\partial^2 w_o}{\partial x\partial y} \end{Bmatrix} \tag{6}$$

The strain-displacement relationships established for Kirchhoff plate theory are now used in developing an inverse-plate element based on the weighted least-squares iFEM formulation.

The newly proposed two-dimensional four-node quadrilateral inverse-plate element, labeled iKP4, is formulated based on Kirchhoff's plate theory assumptions. The formulation employs cubic Hermite basis functions to model thin plate bending behavior within the framework of iFEM. Hermite basis functions are essential because they include deflection and slope continuity across the elements, which is crucial for accurately modeling the bending behavior of thin plates.

In this formulation, a subparametric approach is adopted. It utilizes C^0 continuous bi-linear basis functions for geometric mapping and C^1 continuous Hermite basis functions for interpolating the bending strain field. This approach not only provides a straightforward and computationally efficient geometric representation but also allows higher-order transverse continuity, a key requirement for precise modeling of the bending behavior of thin plates.

In contrast to isoparametric formulations, usually based on shear deformation theories, the inclusion of drilling rotation in the proposed subparametric approach does not guarantee consistent treatment of rotations due to different interpolation functions used for mapping geometric and field variables. Therefore, analyzing curved shell structures would necessitate an artificial in-plane rotation technique, which is a common practice in FEM and iFEM analyses.

Consider a four-node quadrilateral inverse-plate element defined in the physical coordinate system (x, y, z) with nodes located at the mid-plane, where $z \in [-t/2, t/2]$ defines the thickness of the element as shown in Figure 1. The master element depicted in Figure 2 is defined in the natural coordinate system (ξ, η).
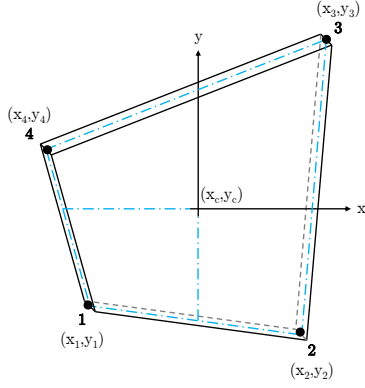
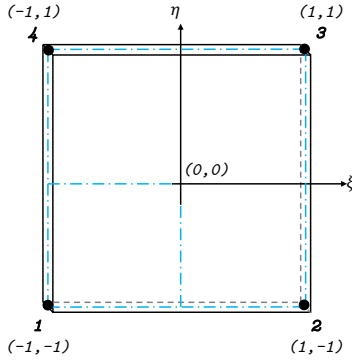**Figure 1:** iKP4 defined in the physical coordinate system

Figure 2: Master element defined in natural coordinate system

The geometrical mapping between physical and natural coordinate systems is achieved using bi-linear basis functions $N_i(\xi, \eta)$ expressed as follows:

$$N_i = \frac{1}{4}\left(1 + \xi_o\right)\left(1 + \eta_o\right) \tag{7}$$

$$\xi_o = \xi\xi_i, \quad \eta_o = \eta\eta_i \quad (i = 1, 2, 3, 4)$$

where ξ_i and η_i denote natural coordinates of the ith node of the element, and the explicit form of bi-linear basis functions is provided in the Appendix. Based on the displacement field given in equation (1) and assumptions of Kirchhoff plate theory, the nodal displacement vector comprises the following 5-DOFs for the proposed iKP4 inverse-plate element.

$$\mathbf{u}_i^e = \begin{Bmatrix} (u_o)_i \\ (v_o)_i \\ (w_o)_i \\ \left(\dfrac{\partial w_o}{\partial x}\right)_i \\ \left(\dfrac{\partial w_o}{\partial y}\right)_i \end{Bmatrix} \quad (i = 1, 2, 3, 4) \tag{8}$$

For the ith node of inverse element, (u_o, v_o, w_o) are the nodal displacements, and $(\frac{\partial w_o}{\partial x}, \frac{\partial w_o}{\partial y})$ are the bending rotations along the y and x axis, respectively. These unknown nodal displacements are computed during iFEM analysis and then interpolated over the elemental domain Ω^{el} to get displacement distribution over the entire element. A common iFEM methodology for inverse element formulation involves the addition of local membrane and bending gradient matrices for the flat homogeneous plates. To begin with, the derivation process of the local membrane gradient matrix is discussed.

The in-plane translational displacement variables u_o and v_o in equation (1) can be described as nodal displacements u_i and v_i using bi-linear basis functions already expressed in equation as (7)

$$u = \sum_{i=1}^{4} N_i \left(u_o\right)_i \tag{9}$$

$$v = \sum_{i=1}^{4} N_i \left(v_o\right)_i \tag{10}$$

Analytical elemental strains $e(\mathbf{u}^e)$ for the membrane part of the formulation can be computed using equation (9) and (10) in equation (5) as

$$e(\mathbf{u}^e) = \mathbf{B}^m \mathbf{u}^e \tag{11}$$

In equation (11), $\mathbf{B}^m$ and $\mathbf{u}^e$ represent the element membrane gradient matrix and displacement vector where nodal membrane gradient matrix B_i^m can be written in terms of the nodal basis functions as:

$$B_i^m = \begin{bmatrix} \dfrac{\partial N_i}{\partial x} & 0 & 0 & 0 & 0 \\ 0 & \dfrac{\partial N_i}{\partial y} & 0 & 0 & 0 \\ \dfrac{\partial N_i}{\partial y} & \dfrac{\partial N_i}{\partial x} & 0 & 0 & 0 \end{bmatrix} \tag{12}$$

Consequently, by using equation (12) for each node ($i = 1, 2, 3, 4$), the local membrane gradient matrix $\mathbf{B}^m$ for the complete element can be computed as follows:

$$\mathbf{B}^m = \begin{bmatrix} B_1^m & B_2^m & B_3^m & B_4^m \end{bmatrix} \tag{13}$$

The formulation of the local bending gradient matrix is now discussed. According to Kirchhoff plate theory, the out-of-plane displacement consists of the transverse deflection and two bending rotations, which are the derivatives of the transverse deflection. Therefore, the Hermite family of interpolation functions is deemed suitable for interpolating the transverse displacement and its derivatives. Non-conforming cubic Hermite basis functions, defined in the

natural coordinate system, are considered for the proposed four-node quadrilateral inverse element. These functions ensure inter-element continuity of the transverse deflections and provide continuity of bending slopes at the element nodes. The explicit form of these basis functions is separately presented in the Appendix; however, in their compact form, these basis functions can be written as:

$$M_i = \frac{1}{8}(1 + \xi_o)(1 + \eta_o)(2 + \xi_o + \eta_o - \xi^2 - \eta^2) \quad (14)$$

$$M_{x_i} = \frac{1}{8}\xi_i(\xi_o - 1)(1 + \eta_o)(1 + \xi_o)^2 \quad (15)$$

$$M_{y_i} = \frac{1}{8}\eta_i(\eta_o - 1)(1 + \xi_o)(1 + \eta_o)^2 \quad (16)$$

$$\xi = \frac{x - x_c}{a}, \quad \eta = \frac{y - y_c}{b} \quad (i = 1, 2, 3, 4)$$

where (ξ_i, η_i) denotes natural coordinates of the ith node of the inverse element with side length 2, and (x_c, y_c) are the global coordinates of the center of the inverse element with $2a$ and $2b$ being the length of its sides. Since the bilinear basis function in equation (7) is still used for the geometric mapping, the formulation for the bending part is sub-parametric. The out-of-plane displacement variables in equation (1) can now be expressed in terms of nodal displacements $(w_o)_i$, $(\frac{\partial w_o}{\partial x})_i$, and $(\frac{\partial w_o}{\partial y})_i$ using cubic basis functions outlined in equation (14), (15), and (16) as:

$$w = \sum_{i=1}^{4} M_i (w_o)_i \quad (17)$$

$$\frac{\partial w}{\partial x} = \sum_{i=1}^{4} M_{x_i} \left(\frac{\partial w_o}{\partial x}\right)_i \quad (18)$$

$$\frac{\partial w}{\partial y} = \sum_{i=1}^{4} M_{y_i} \left(\frac{\partial w_o}{\partial y}\right)_i \quad (19)$$

Similar to the membrane part, analytical elemental strains $\kappa(u^e)$ for the bending part can be computed using equations (17), (18) and (19) in equation (6) as

$$\kappa(u^e) = \mathbf{B}^b u^e \quad (20)$$

where $\mathbf{B}^b$ in equation (20) represents the element bending gradient matrix; then, the nodal bending gradient matrix B_i^b can be written in terms of the nodal Hermite basis functions as:

$$B_i^b = \begin{bmatrix} 0 & 0 & -\dfrac{\partial^2 M_i}{\partial x^2} & -\dfrac{\partial^2 M_{x_i}}{\partial x^2} & -\dfrac{\partial^2 M_{y_i}}{\partial x^2} \\[2mm] 0 & 0 & -\dfrac{\partial^2 M_i}{\partial y^2} & -\dfrac{\partial^2 M_{x_i}}{\partial y^2} & -\dfrac{\partial^2 M_{y_i}}{\partial y^2} \\[2mm] 0 & 0 & -2\dfrac{\partial^2 M_i}{\partial x \partial y} & -2\dfrac{\partial^2 M_{x_i}}{\partial x \partial y} & -2\dfrac{\partial^2 M_{y_i}}{\partial x \partial y} \end{bmatrix}$$
$$(21)$$

Finally, the local bending gradient matrix $\mathbf{B}^b$ can be calculated by concatenating B_i^b for each node ($i = 1, 2, 3, 4$) of the iKP4 inverse-plate element as

$$\mathbf{B}^b = \begin{bmatrix} B_1^b & B_2^b & B_3^b & B_4^b \end{bmatrix} \quad (22)$$

The iFEM framework is built on the principle of the variational method, where the displacement field is reconstructed by minimizing the weighted least squares error functional. The error functional is formulated using discrete strain measures and their corresponding FEM counterparts in a discretized geometric space. One of the significant benefits of the iFEM scheme is its independence from elastic or inertial material properties and loading conditions for full-field shape reconstruction.

The weighted least squares functional for the proposed iKP4 element is defined as the sum of the error terms between the numerically calculated and discretely measured values of the membrane and bending strains as

$$\phi^e(u^e) = w_e \left\| e(u^e) - e^* \right\|^2 + w_k \left\| \kappa(u^e) - \kappa^* \right\|^2 \quad (23)$$

where $e(u^e)$ and $\kappa(u^e)$ represent analytically computed elemental membrane and bending strains. In contrast, e^* and κ^* indicate in-situ discrete strain measures obtained from the strain sensors located in the discretized elemental geometric domains; w_e and w_k are the weighting coefficients associated with the error functional corresponding to membrane and bending errors, respectively.

Each of the squared norms defined in equation (23) can be further expressed over the inverse element domain Ω^{iel} as:

$$\left\| e(u^e) - e^* \right\|^2 = \iint_{A_e} \left(e(u^e) - e^* \right)^2 dx dy \quad (24)$$

$$\left\| \kappa(u^e) - \kappa^* \right\|^2 = t^2 \iint_{A_e} \left(\kappa(u^e) - \kappa^* \right)^2 dx dy \quad (25)$$

where A_e is the element's area. Discrete in-situ strain measurements obtained from sensors are pivotal in iFEM formulation. Using these discrete strain measures, experimental section strains can be computed at n discrete locations (x_j, y_j) in the plate's mid-plane as shown in Figure 3.

Since the iKP4 inverse-plate element is developed for general loading conditions exhibiting mixed in-plane and out-of-plane loads, both top and bottom stain sensors are needed for general iFEM analysis. However, strain sensors on either the top or bottom sides can suffice the requirements for plane stress and pure bending cases. Hence, in-situ strain data obtained from the plate's top and bottom surfaces can be represented in vector forms, constituting discrete measurements for membrane and bending strains as:
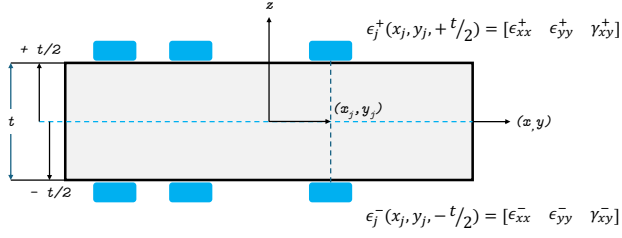
Figure 3: Strain rosettes at discrete locations $(x_j, y_j, \pm\frac{t}{2})$

$$e_j^* = \frac{1}{2}\left\{\begin{array}{c} \varepsilon_{xx}^+ + \varepsilon_{xx}^- \\ \varepsilon_{yy}^+ + \varepsilon_{yy}^- \\ \gamma_{xy}^+ + \gamma_{xy}^- \end{array}\right\} \quad (j = 1, n) \tag{26}$$

$$\tag{27}$$

$$\kappa_j^* = \frac{1}{t}\left\{\begin{array}{c} \varepsilon_{xx}^+ - \varepsilon_{xx}^- \\ \varepsilon_{yy}^+ - \varepsilon_{yy}^- \\ \gamma_{xy}^+ - \gamma_{xy}^- \end{array}\right\} \quad (j = 1, n) \tag{28}$$

where e_j^* and κ_j^* represent discrete strain data obtained at (x_j, y_j) location. The variable n accounts for the number of sensor locations per element; superscripts $^{(+)}$ and $^{(-)}$ associate the strain measures with the strain rosettes located on the top and bottom surfaces of the plate, respectively. For practical reasons, experimental strains in one inverse element do not exceed $n = 1$.

The values for the weighting coefficients w_e and w_k, already defined in the least squares functional in equation (23), can be specified based on the availability of discrete strain data. The values for the weighting coefficients can be set to unity; that is, $w_e = w_k = 1$ if discrete strain measures (e_j^*, κ_j^*) are available within the given element domain. Otherwise, the values for w_e and w_k are assumed to be minimal, i.e., $(w_e, w_k) \ll 1$, if the discrete strain data is missing in the element domain.

During the least squares error minimization process, these weighting coefficients help to balance the influence of available discrete strain measures in the closed-form solution. Setting the coefficients to unity ($w_e = w_k = 1$) gives equal importance to all data points, which are known with certainty when the strain measures are available. On the other hand, setting the coefficients to a minimal value ($w_e = w_k = 10^{-3}$ to 10^{-6}) when the strain data is missing reduces the impact of these missing data points during the error minimization process, preventing them from unduly affecting the overall result. This approach helps to ensure that the iFEM algorithm exhibits robustness and reliability in computing displacement profiles even with sparse arrangements of strain sensors, making them valuable for real-world shape-sensing and SHM applications.

Minimizing the weighted least squares error functional in equation (23) with respect to the unknown nodal displacements u^e of an inverse element reduces to the normal equation of the form:

$$\frac{\partial \boldsymbol{\phi}^e(u^e)}{\partial u^e} = k^e u^e - f^e = 0 \tag{29}$$

$$k^e u^e = f^e \tag{30}$$

In equation (30), k^e represents the local numerical shape matrix (inverse element stiffness matrix), f^e is the local experimental shape vector (inverse element force vector), and u^e are element displacements to be determined after prescribing necessary displacement boundary conditions. The mathematical expressions for k^e and f^e can be further derived by substituting equation (11) and (20) in (29) as:

$$k^e = \iint_{A_e}\left(w_e(\mathbf{B}^m)^T\mathbf{B}^m + (t^2)w_k(\mathbf{B}^b)^T\mathbf{B}^b\right)dx\,dy \tag{31}$$

$$f^e = \iint_{A_e}\left(w_e(\mathbf{B}^m)^T e^* + (t^2)w_k(\mathbf{B}^b)^T \kappa^*\right)dx\,dy \tag{32}$$

Next, the global system of equations can be formulated based on the element contributions given in equations (31) and (32) as:

$$\mathbf{KU} = \mathbf{F} \tag{33}$$

$$\text{and} \quad \mathbf{K} = \sum_{e=1}^{N_{iel}} k^e, \quad \mathbf{U} = \sum_{e=1}^{N_{iel}} u^e, \quad \mathbf{F} = \sum_{e=1}^{N_{iel}} f^e$$

where N_{iel} is the total number of inverse elements. After prescribing the essential boundary conditions, the partitioned global system of equations can be written as:

$$\mathbf{K}_p \mathbf{U}_p = \mathbf{F}_p \tag{34}$$

Consequently, $\mathbf{K}_p$, $\mathbf{U}_p$, and $\mathbf{F}_p$ implies the prescribed global inverse stiffness matrix, unknown displacement vector, and global inverse force vector in iFEM formulation. In the end, unknown nodal displacements can be calculated by following conventional FEM approaches to realize full-field reconstruction of shape-sensing and stress profiles for iFEM analysis.

3. Numerical Validation

The iFEM formulation of the proposed inverse-plate element is numerically validated by considering various case studies in the following section. A detailed numerical validation plan includes plate structures under in-plane (plane stress), out-of-plane (pure bending), and mixed in-plane and out-of-plane (general) loading conditions. In the next section, defect resolution cases are also considered based on similar numerical approaches followed in the subsequent numerical analysis.

Numerical modelling is extensively used in research and development sectors to simulate real-world phenomena. All numerical models are based on certain assumptions or simplifications; therefore, their validation against analytical solutions helps to verify the validity of these assumptions and ensures that they do not introduce significant errors. This is crucial for ensuring that the numerical results are reliable and can be used confidently for real-world applications.

On the contrary, if analytical solutions are not readily available for more general cases, establishing an equivalent structural state is mandatory for numerical validation. As a consequence, the computation of equivalent displacements can help to validate iFEM results against FEM reference solutions. The total equivalent displacement of the iKP4 inverse-plate can be computed as:

$$U_{eq} = \sqrt{u^2 + v^2 + w^2} \tag{35}$$

where u, v, and w are the longitudinal, lateral, and transverse plate displacements along the x, y, and z axis. Furthermore, to investigate the accuracy of iFEM results, the percent-difference between the reconstructed displacements (i.e., equivalent displacements) profile and FEM reference solution can be calculated as:

$$Percent\ Difference\ (\%) = \left| \frac{U_{eq}^{iFEM} - U_{eq}^{Ref}}{U_{eq}^{Ref}} \right| \times 100 \tag{36}$$

and variables U_{eq}^{iFEM} and U_{eq}^{Ref} imply equivalent displacements computed via iFEM analysis and its reference solution computed through high-fidelity FEM analysis.
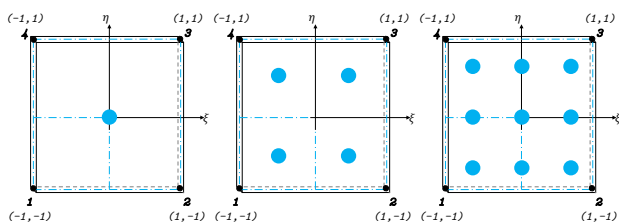

Figure 4: 1, 2 and 3 point Gauss locations in master element

The availability of discrete surface strain measures is an integral part of the iFEM analysis, and the kind of data is obtained from the strain sensor networks in real-world applications. In the current study, this data is obtained via high-fidelity FEM simulations, which is equivalent to the placement of the strain rosette at an appropriate location in the iFEM discretized element.

The discrete location of strain sensors at the inverse element domain is critical in iFEM analysis, and sensor location optimization is an ongoing area of active research. The strain rosette can be placed anywhere within the inverse element domain for iFEM analysis; some direct options are Gauss point locations, as depicted in Figure 4. The discrete locations can be optimized differently depending upon various factors, such as the geometric construction of engineering structure, type of loading conditions, critical stress areas, etc. For this research, the location of the strain rosette within the master element domain is fixed at its center (single point Gauss location) for all numerical validation cases under discussion.

In addition to sensor locations, the weighting coefficients w_e and w_k defined in equation 23 are equally important in minimizing the weighted least squares error functional. For missing in-situ discrete strain measures, the values are set to minimal, i.e., $w_e = w_k << 1$, and the acceptable range can vary usually between 10^{-3} to 10^{-6}. However, to ensure adequate standardization in numerical results interpretation, w_e and w_k are set to 10^{-4}. Though sensor location and weighting functions are crucial to the variational formulation of iFEM, their fixation enables comparative error analysis among various cases considered for numerical validation.

In industrial applications, the decision on the number of sensors needed for shape sensing is governed by several factors. These include the availability of space for sensor installation, financial constraints, existing health of the structural systems, computational accuracy, and efficiency requirements. Optimal sensor arrangement can be achieved by optimizing the iFEM scheme for inverse element discretization, sensor locations within the inverse element spatial domain, and weighting functions associated with the weighted least squares error functional. Additionally, techniques such as sensor fusion and advanced signal processing can further enhance the robustness of iFEM analysis with fewer sensors. It is important to note that these optimizations are specific to each structure subjected to its unique in-service loading conditions. Therefore, in industrial applications, separate optimization, and desirability studies are performed for each structural system to attain optimal arrangement for onboard sensors. Therefore, a unique closed-form solution does not exist to obtain an optimal sensor arrangement.

In subsequent numerical cases, sparse sensor arrangements are arbitrarily assumed to have a significantly reduced number of sensors compared to dense sensor arrangements. The aim, however, remains to analyze the capability and robustness of the proposed iFEM formulation using fewer sensors while keeping all other variable factors constant, i.e., discretization, sensor locations, and weighting functions. This approach minimizes variations and simplifies comparative analysis of iFEM results across different numerical validation cases.

3.1. In-plane Loading (Case - I)

A plane stress case is the most straightforward of the two-dimensional structural analysis. Analytical solutions are available for various problems considering the application of point loads and edge traction. Numerous authors [37, 38] use the shear-loaded cantilever beam to validate the membrane response of new elements. Herein, this problem is reconsidered to access the membrane response capability of the newly developed iKP4 inverse-plate element.
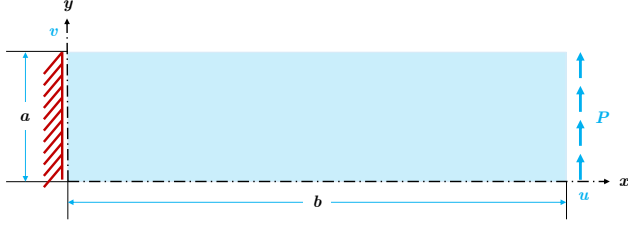

Figure 5: Cantilevered beam - free edge under shear load

A rectangular beam of length $a = 1.2192\ m$ and width $b = 0.3048\ m$ has a constant cross-sectional area with thickness $t = 25.4\ mm$. The left edge of the beam is fixed, and the right edge is subjected to resultant shear loading $P = 177.929\ kN$ as shown in Figure 5. The beam is made of uniform and isotropic material with the elastic modulus $E = 206.84\ GPa$ and Poisson's ratio $v = 0.25$.

The elasticity solution [39] for the maximum vertical displacement at the upper tip of the free edge is given as:

$$V = \frac{4Pa^3}{Etb^3} + \frac{2(4 + 5v)Pa}{4Etb} = 9.025\ mm \qquad (37)$$

First, the high-fidelity FEM analysis was performed by using an in-house FEM solver, and the mesh with 1024 uniformly distributed square elements converges to the analytical solution obtained in equation 37. The maximum V_y displacement obtained from the FEM analysis is 9.039 mm, which agrees well with the analytical solution. Two iFEM analyses follow this; the first considers dense-sensor arrangement, whereas the second is based on the more practical sparse-sensor arrangement. Figure 6 shows the FEM mesh, iFEM dense-sensor arrangement, and iFEM sparse-sensor arrangement for the current case.

Numerical validation is performed using two different iFEM beam analyses depending on the sensor arrangement. For the dense sensor arrangement, it is considered that strain rosettes are placed in all inverse-element domains. In contrast, for sparse-sensor arrangement, the strain rosettes are placed in selected inverse-element domains along the plate boundary and mid-way along plate length and width dimensions, as highlighted in Figure 6. For both iFEM scenarios, the surface strains are computed via high-fidelity FEM deflections. In-plane loading conditions necessitate strain data for any surface of the plate (either top or bottom) because the resulting membrane deformations are constant
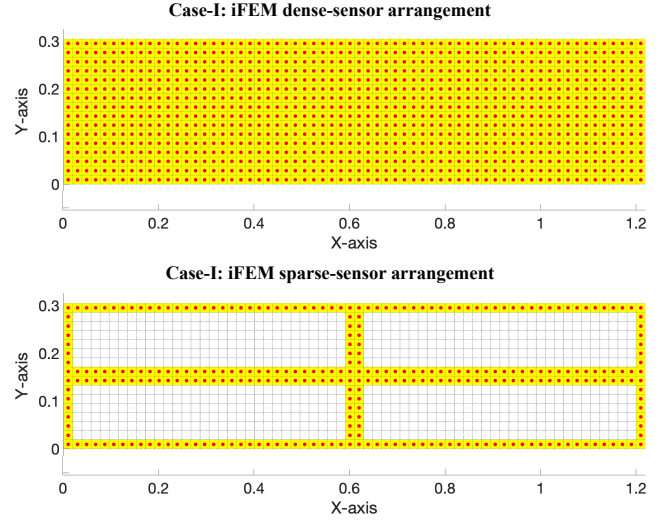

Figure 6: Case-I : iFEM dense-sensor arrangement, and iFEM sparse-sensor arrangement

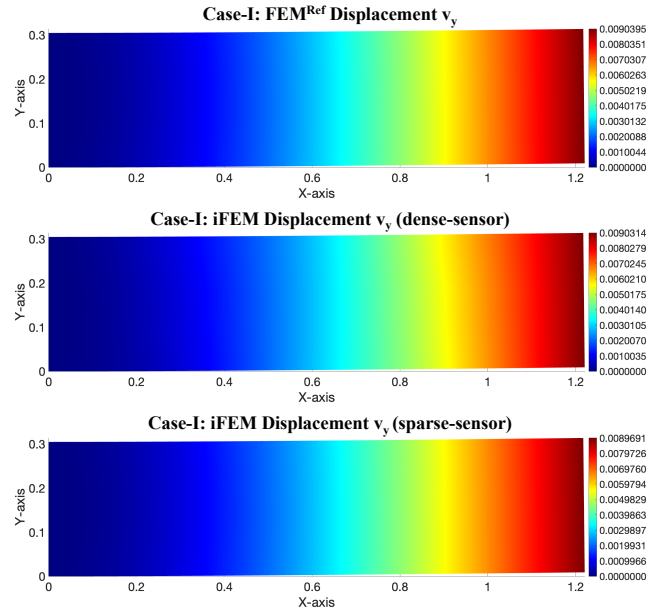through the thickness of the plate for homogeneous isotropic materials.

Figure 7: Case-I : Vertical Displacement Profiles for FEM^Ref solution, iFEM solution (dense-sensor), and iFEM solution (sparse-sensor)

The vertical displacement profile from two different iFEM analyses produces very close results for maximum vertical displacement for a shear-loaded cantilever beam, as shown in Figure 7. The comparison of maximum vertical displacement against the analytical result (in equation 37) shows an error of 0.066% and 0.620% for dense and sparse iFEM analysis. FEM and iFEM vertical displacements are in excellent agreement with each other showing the maximum deflection at the right edge of the cantilever beam. The analysis details for Case-I are summarised in Table 1.

Table 1
Analysis details of Case - I.

Analysis	Sensors	Max $\mathbf{v_y}$	Max $\mathbf{u_x}$	Error [$\mathbf{v_y}$]
FEM	- - - - -	9.039 mm	1.634 mm	−0.155%
iFEM	Dense	9.031 mm	1.624 mm	−0.066%
iFEM	Sparse	8.969 mm	1.620 mm	+0.620%
Analytical Solution [39] 9.025 mm				

Table 2
Analysis details of Case - II.

Analysis	Sensors	Max $\mathbf{w_z}$	Error [$\mathbf{w_z}$]
FEM	- - - - -	−0.9229	−0.043%
iFEM	Dense	−0.9219	+0.065%
iFEM	Sparse	−0.9257	−0.346%
Analytical Solution [40] −0.9225			

Analysis of the in-plane loading case establishes the precision of the iKP4 inverse-plate element in the accurate reconstruction of horizontal and vertical displacement profiles using dense and sparse sensor arrangements.

3.2. Out-of-plane Loading (Case - II)

Numerical validation for the pure bending case is accomplished by reconsidering a classical textbook problem presented by Reddy [40] using the iKP4 inverse-plate element within the framework of iFEM. An orthotropic square plate of graphite-epoxy with simply supported boundary conditions is considered under arbitrary uniform transverse pressure q_o as shown in Figure 8. The length a, width b, and thickness t of the plate can be chosen arbitrarily because the validation is performed based on dimensionless parameters, i.e., $a = b = c$ and $t \ll c$, where c is the characteristic length of the plate. Material properties for the plate with fiber direction $'1'$ aligned along the global x-axis are as follows.

$$E_1 = 31.8 \text{ Mpsi}, \quad E_2 = 1.02 \text{ Mpsi}$$
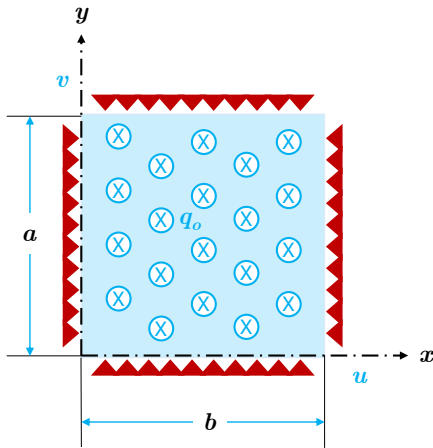$$G_{12} = 0.96 \text{ Mpsi}, \quad \nu_{12} = 0.31$$

Figure 8: Simply supported square plate under arbitrary uniform transverse load

Under given boundary conditions, the maximum dimensionless transverse deflection at the center of the plate is:

$$\bar{w}_{max} = w \times 10^3 \times \frac{D_{12} + 2D_{66}}{q_o a^4} = -0.9225 \quad (38)$$

For the pure bending case, the numerical validation of the iKP4 inverse-plate element is also performed by using two different iFEM analyses. A dense sensor arrangement in iFEM analysis is necessary for analytical validation, whereas a sparse sensor arrangement determines the robustness of the iFEM analysis for real-time applications, as depicted in Figure 9.
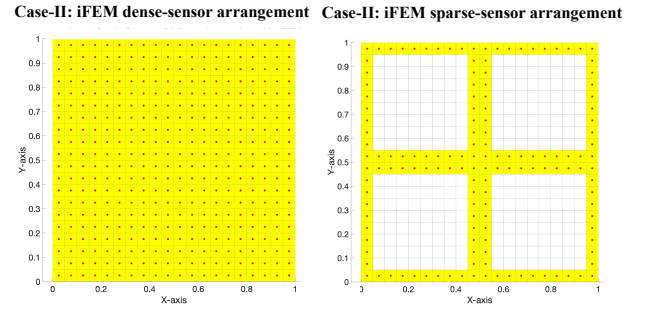

Figure 9: Case-II : iFEM dense-sensor arrangement, and iFEM sparse-sensor arrangement

At first, a high-fidelity FEM analysis was performed by using an in-house FEA package which convergence to the analytical solution utilizing 400 elements for the numerical case is under discussion. A normalized maximum out-of-plane displacement of −0.9229 was observed at the center of the supported plate, which agrees with the analytical value of −0.9225 obtained in equation 38. Surface strains are then computed through FEM transverse deflections for iFEM analyses. Also, for the pure bending cases, experimental strain data on any of the plate surfaces (top or bottom) is sufficient for subsequent iFEM analysis.

The dimensionless transverse displacements obtained from iFEM analyses closely conform to the analytical solution, with an error of 0.065% for iFEM analysis under a dense sensor arrangement and 0.346% for iFEM analysis under a sparse sensor arrangement for a supported plate subjected to a distributed transverse load. For the current case, the details of the iFEM analysis are tabulated hereafter in Table 2.

The comparison of FEM and iFEM displacement contours in Figure 11 shows an accurate prediction of normalized out-of-plane displacements, demonstrating the superior capability of the iKP4 inverse-plate element in reconstructing accurate deformation profiles for pure bending cases.

Furthermore, the higher C^1 continuity of Hermite basis functions enables coarser inverse discretization to predict the bending behavior of thin plates without significantly
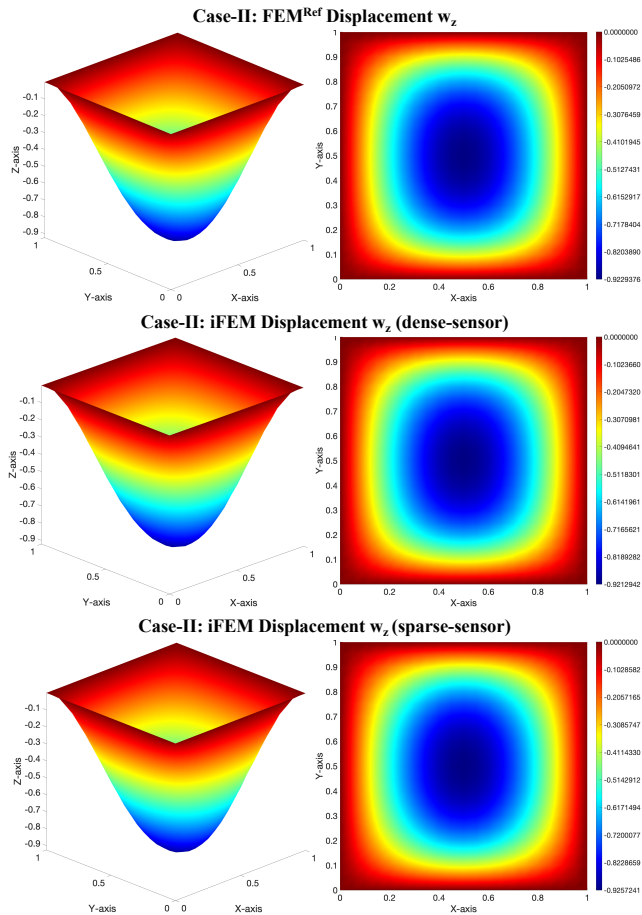
Figure 10: Case-II : Transverse Displacement Profiles for FEM^Ref solution, iFEM solution (dense-sensor), and iFEM solution (sparse-sensor)
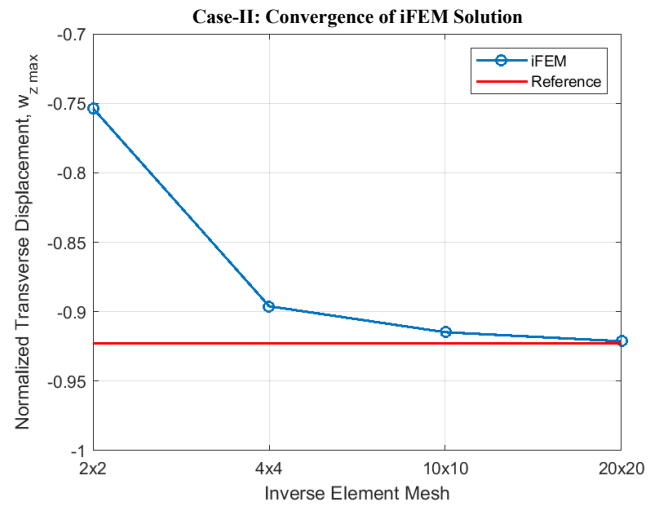

Figure 11: Case-II : Influence of discretization on iFEM analysis

edges of the plate to generate a torsional moment in the plate, as shown in Figure 12. The orthotropic material properties of the unidirectional graphite-epoxy [41] plate with fiber direction $'1'$ aligned with the global x-axis are as follows.

$$E_1 = 181.0\,GPa, \quad E_2 = 10.3\,GPa, \quad E_3 = 10.3\,GPa$$
$$G_{12} = 7.17\,GPa, \quad G_{31} = 7.17\,GPa, \quad G_{23} = 5.96\,GPa$$
$$v_{12} = 0.277, \quad v_{31} = 0.016, \quad v_{32} = 0.4$$
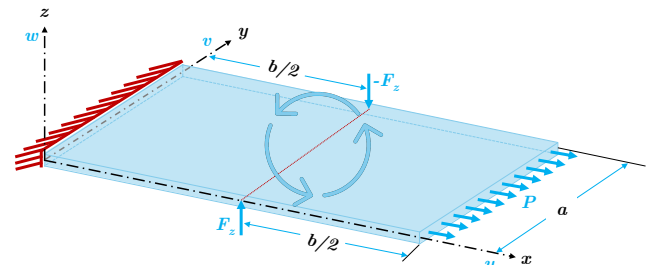
Figure 12: Cantilevered beam under mixed in-plane traction and out-of-plane torsional loading condition

compromising the accuracy of iFEM analysis. In Figure 11, a convergence graph displays a horizontal line representing the reference solution alongside a blue line depicting the iFEM solution for various discretization levels indicated on the x-axis. The convergence chart clearly illustrates that the iFEM solution monotonically converges to the reference solution as the number of elements in the geometric domain increases. More importantly, for a 4×4 mesh arrangement, the accuracy of iFEM analysis is $\approx 95\%$ while keeping all other variational factors constant. Optimizing sensor locations and weighting functions within the iFEM framework allows for improved accuracy even with significantly coarser discretization.

3.3. General Loading (Case - III)

After validating plane stress and pure bending cases, a general loading condition, i.e., mixed in-plane and out-of-plane loading, is now considered for the thin plate of similar geometric dimensions as considered for the beam in Case-I but fabricated from unidirectional graphite-epoxy. The plate is fixed on its left edge, and the free edge is subjected to a traction of $P = 177 \times 10^6\,N/m$. Additionally, a couple of point load $F_z = \pm 17.7\,kN$ are applied at the top and bottom

The general loading case under discussion is again numerically validated by considering two iFEM analyses for dense and sparse sensor arrangements, as shown in Figure 13. In the sparse-sensor arrangement, strain data is considered only on the boundary of the plate structure. Initially, the FEM analysis of the plate was performed by using an in-house FEA package, and the converged solution shows mesh independence at 1024 quadrilateral elements. The maximum horizontal and transverse displacement of $u_x = 4.42\,mm$ and $w_z = 27.8\,mm$ is observed at the free edge of the plate under in-plane traction and out-of-plane torsional loading conditions. Simulated discrete strain measures are obtained from FEM displacements for their subsequent application during iFEM analysis. In the case of mixed loading conditions, i.e.,

the presence of in-plane and out-of-plane loads, the sensor strain data is acquired from both (top and bottom) surfaces of the plate structure.
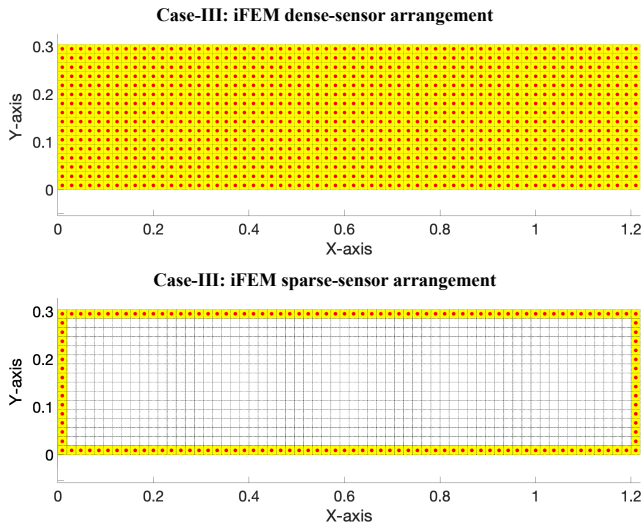

Figure 13: Case-III : iFEM dense-sensor arrangement, and iFEM sparse-sensor arrangement

Numerical validation for mixed loading case is performed against the high-fidelity FEM reference solution, and the error estimations are performed based on equivalent displacements expressed in equation 36. The horizontal displacement profiles of the FEM analysis and the two different iFEM setups are entirely indistinguishable, as shown in Figure 14. Maximum horizontal displacements obtained from dense and sparse iFEM analysis are equivalent to FEM maximum displacement of $u_x = 4.42\ mm$, thus rendering negligible errors for a complete horizontal displacement profile.

In the presence of equal and opposite transverse point loads, the plate is subjected to out-of-plane torsion and thus generates symmetric transverse deformation. The transverse displacement profiles obtained from iFEM analysis accurately predict the twisting behavior of the plate, as evident from Figure 15. A maximum transverse displacement of 27.80 mm and 27.76 mm is observed for dense and sparse sensor iFEM configurations which are very close to the maximum transverse displacement of 27.81 mm obtained from high-fidelity FEM solution. For both iFEM configurations, the transverse displacement contours show symmetric twisting of the plate as observed in the FEM reference solution.

The contour plots for bending rotations are also observed as a perfect match against the FEM reference solution; they are not discussed here for the brevity of the discussion. However, these plots will be discussed in detail during defect resolution analysis in the next section. The details of FEM and iFEM analysis for general loading case are highlighted in Table 3.

Excellent conformance of the iFEM solutions against the analytical and FEM reference solution determines the
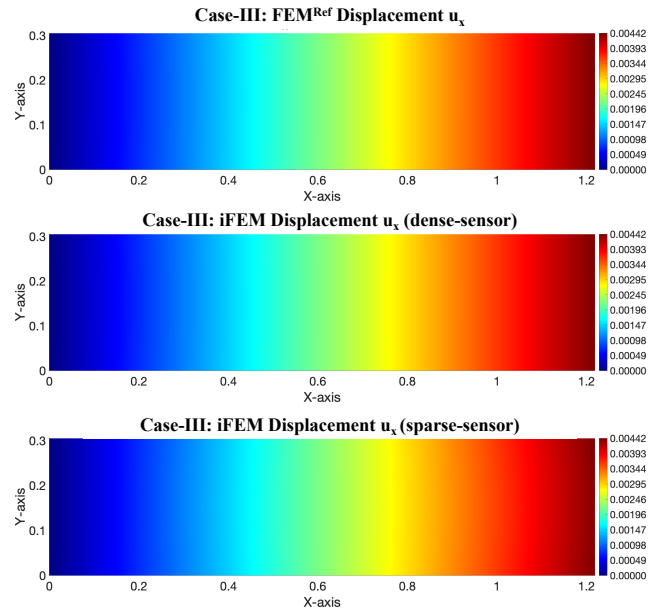

Figure 14: Case-III : Horizontal Displacement Profiles for FEM^{Ref} solution, iFEM solution (dense-sensor), and iFEM solution (sparse-sensor)
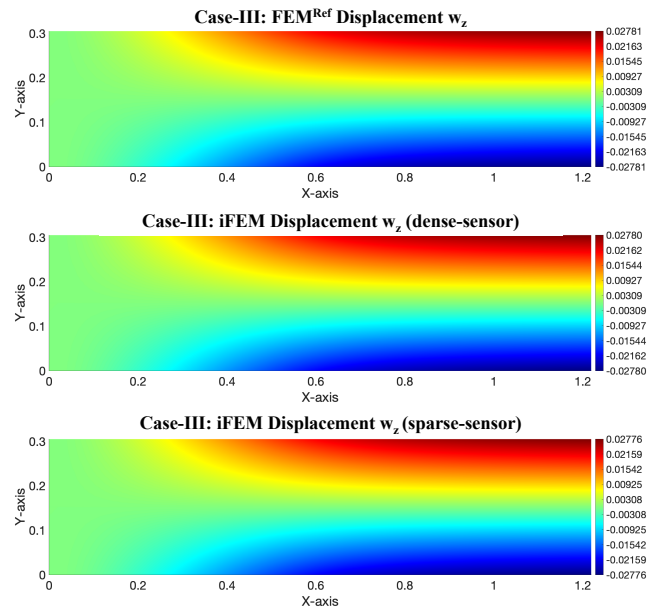

Figure 15: Case-III : Transverse Displacement Profiles for FEM^{Ref} solution, iFEM solution (dense-sensor), and iFEM solution (sparse-sensor)

superior capability of the iKP4 inverse-plate element for the full-field reconstruction of deformation profiles. Hence, the proposed inverse-plate element formulation based on discrete Kirchhoff assumptions can be confidently used for thin plate structures in real-time shape-sensing and SHM applications.

Table 3
Analysis details of Case - III.

Analysis	Sensors	u_x^{max}	w_z^{max}	Error [U_{eq}]
FEM	- - - - -	4.42 mm	27.81 mm	Ref Sol
iFEM	Dense	4.42 mm	27.80 mm	< 0.01%
iFEM	Sparse	4.42 mm	27.76 mm	< 0.01%
Validation against FEM Reference Solution				

4. Defect Resolution Analysis

After successful numerical validation of the proposed iKP4 inverse-plate element in shape-sensing aspects, its defect detection capability is now analyzed for SHM applications. The term defect resolution is frequently used in non-destructive testing (NDT) techniques to represent the resolution potential of an NDT procedure in detecting single or multiple defects. Similarly, implementing the current iFEM formulation in SHM necessitates an in-depth analysis of its defect resolution capability. For numerical defect resolution analysis, this study considers three plate specimens subjected to two different loading conditions, i.e., in-plane and out-of-plane. Defect modeling for the current research is performed in two different ways, that is, by considering geometric discontinuity and by implementing material degradation factor in high-fidelity FEM solutions.

Geometric discontinuities commonly represent defects that are usually evident on the surface of plate structures with distinct geometric definitions, e.g., holes, tears, etc. On the contrary, material property degradation in the domains of subsurface defects, e.g., porosity, and inclusions, can happen when structures are exposed to in-service loading and environmental conditions. Complete characterization of such subsurface defects is often performed by employing appropriate NDT methods; however, their consequence in the form of stiffness reduction in the structure can be modeled using the material degradation factor technique.

4.1. Tensile Loading of Plate

In the first case of tensile loading, two plate specimens are considered to have a geometric discontinuity in the form of a hole at the center of the thin steel plates. Isotropic material properties considered for the plates are $E = 200\,GPa$ and $v = 0.3$. The thickness $t = 0.0001\,m$ of the steel plates is sufficiently small compared to the length $a = 0.03\,m$ and width $b = 0.01\,m$ of the plates, as shown in Figure 15. As represented in their respective figures, symmetric boundary conditions restricting horizontal and vertical translations are applied along red and green lines. Both the plates are subjected to traction of $P = 1.2 \times 10^6\,N/m$ on their left and right free edges.

A larger hole in Plate-A does not necessarily represent a discontinuity. Still, it is considered here for defect resolution comparison against Plate-B, which is modeled with a small punch hole of radius $r = 0.0001\,m$ as geometric discontinuity. First, the plates are analyzed via a high-fidelity FEM
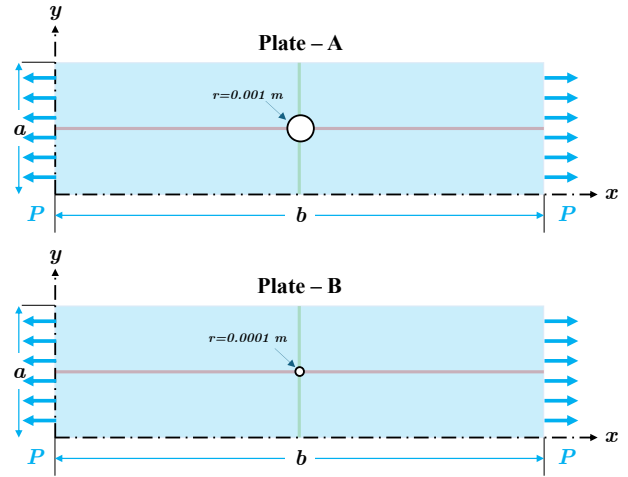

Figure 16: Tensile Loading : Defect analyses configurations for Plate-A, and Plate-B

analysis by using an in-house FEA package, and discrete surface strains are computed for defect resolution analysis within the framework of iFEM. After successful numerical validation of the iKP4 inverse-plate element in the previous section, solutions for only sparse-sensor arrangement iFEM are discussed here for more focused defect analysis. The sparse-sensor arrangements for both plates considered in the defect resolution analyses are shown in Figure 17.
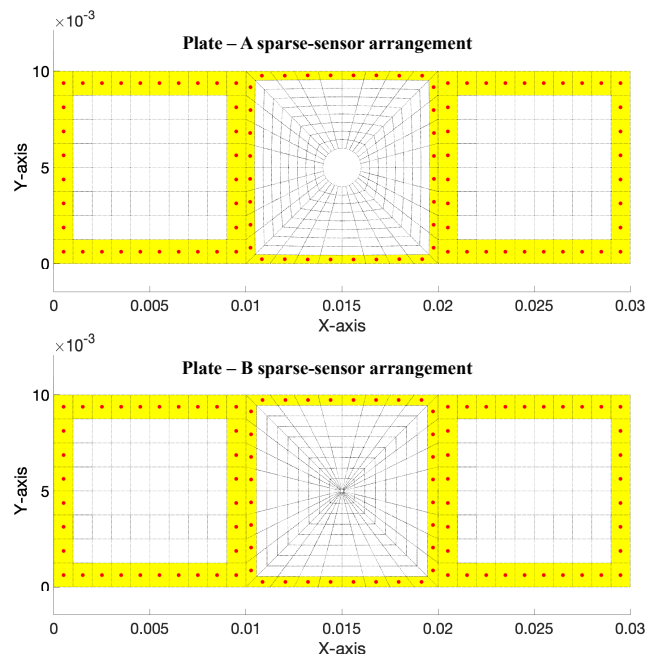

Figure 17: Tensile Loading : iFEM sparse-sensor arrangement for Plate-A, and Plate-B

Horizontal displacement profiles for Plate-A and Plate-B are compared in Figure 18, showing noticeable differences in displacement contours around geometric holes. Notably,

Plate A exhibits a significant variation in displacement contours around a larger geometric hole. However, Plate B is less sensitive to displacement variations because of the minute nature of the discontinuity (punched hole).
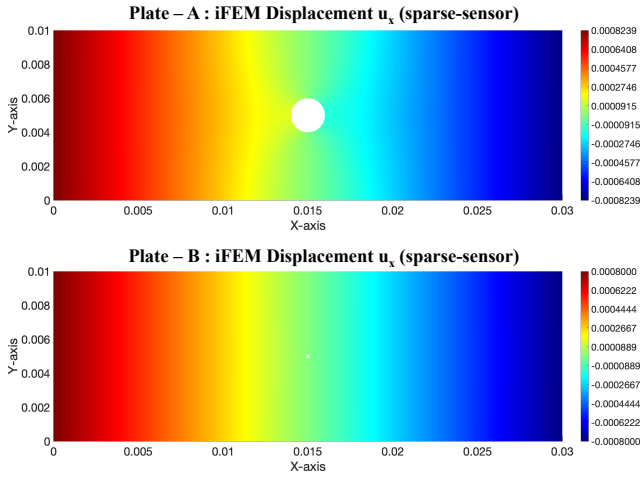

Figure 18: Tensile Loading : Horizontal displacement profiles for Plate-A, and Plate-B

Similarly, the vertical displacement profile of Plate-A quantifies the size of the larger geometric hole because of the distinct variations of displacement contour, as shown in Figure 19. In contrast, the minor discontinuity in the form of a punch hole remains indistinguishable in Plate B, rendering the punch hole more difficult to quantify in reconstructed shape-sensing displacement profiles.
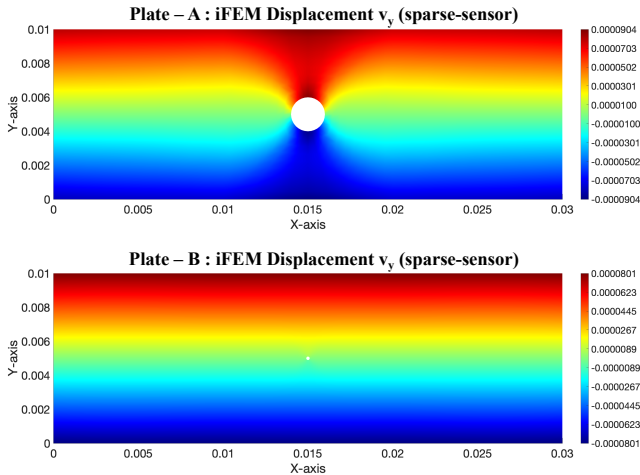

Figure 19: Tensile Loading : Vertical displacement profiles for Plate-A, and Plate-B

To overcome this difficulty, equivalent von Mises strains can be plotted to identify and quantify minor discontinuities, i.e., punch holes in Plate-B. The equivalent von Mises strains can be computed using the following mathematical expression.

$$\varepsilon_{vm} = \sqrt{(\varepsilon_1)^2 - \varepsilon_1 \varepsilon_2 + (\varepsilon_2)^2} \tag{39}$$

where, ε_1 and ε_2 can be calculated as:

$$\begin{cases} \varepsilon_1 &= \frac{\varepsilon_{xx}+\varepsilon_{yy}}{2} + \sqrt{\left(\frac{\varepsilon_{xx}-\varepsilon_{yy}}{2}\right)^2 + \left(\frac{\gamma_{xy}}{2}\right)^2} \\ \varepsilon_2 &= \frac{\varepsilon_{xx}+\varepsilon_{yy}}{2} - \sqrt{\left(\frac{\varepsilon_{xx}-\varepsilon_{yy}}{2}\right)^2 + \left(\frac{\gamma_{xy}}{2}\right)^2} \end{cases}$$
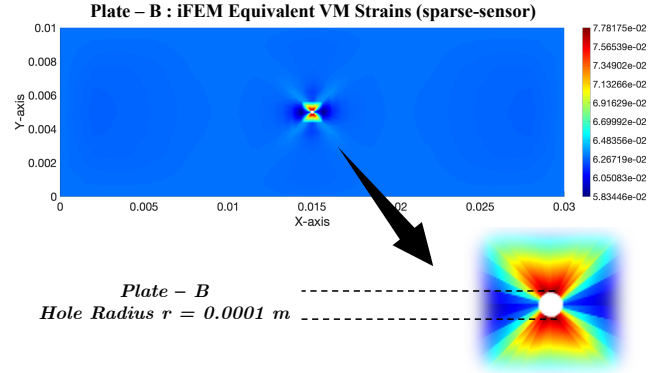

Figure 20: Tensile Loading : Equivalent von Mises strains contour for Plate-B

The von Mises strain contour plot is obtained from iFEM analysis of Plate-B under sparse-sensor arrangement and is depicted in Figure 20. The region of high von Mises strain gradient accurately predicts the location of the punch hole in Plate-B. An in-depth evaluation of the von Mises contour can also help to quantify the geometric discontinuity. Therefore, the equivalent von Mises strain contour demonstrates the defect resolution potential of the iKP4 inverse-plate element in resolving minute geometric discontinuities in thin plate structures.

4.2. Transverse Loading of Plate

In real-world SHM applications, not all defects appear as geometric discontinuities, as discussed in the previous tensile loading case. Most of the subsurface defects appear as a region with lesser stiffness than the overall stiffness of the engineering structure. These defect domains can be modeled by introducing an appropriate damage degradation factor λ, i.e., $0 < \lambda < 1$ where $\lambda = 1$ represents a healthy structural state withholding its material properties, and $0 < \lambda < 1$ corresponds to the degraded state of the material in the structure because of latent subsurface defects. In forward FEM analysis, the material degradation factor λ is incorporated in the element stiffness formulation to model the degraded stiffness matrix. Mathematically, the degraded element stiffness matrix can be expressed as:

$$K_e^d = \lambda(I \odot K_e) \tag{40}$$

In this equation, K_e^d represents the degraded element stiffness matrix; K_e is the element stiffness matrix of intact structure, and I is an identity matrix of the same order

as K_e. The identity matrix ensures accurate element-wise multiplication of degradation factor λ with the diagonal elements of element stiffness matrix K_e. In the present case of transverse loading, defect modeling in the thin plate structure is accomplished within the forward FEM process using equation 40.
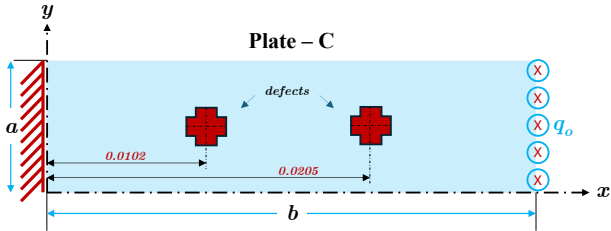

Figure 21: Transverse Loading : Defect analysis configurations for Plate-C

Now, consider a Plate-C with similar dimensions and material properties as Plate-A and Plate-B in the tensile testing case; two defects of a similar nature and size are modeled at the center of Plate-C at varying lengths, as shown in Figure 21. The plate is fixed on its left edge, and a uniform transverse bending load $q_o = 10 \ N/m$ is applied on its free edge.
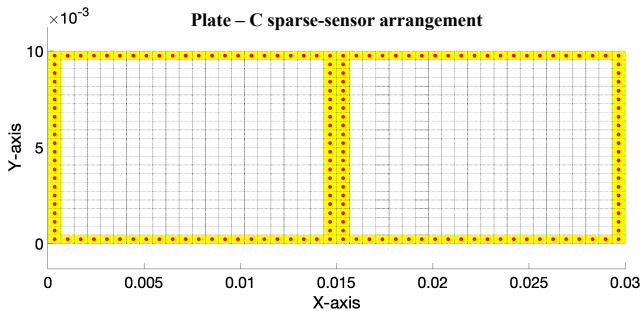

Figure 22: Transverse Loading : iFEM sparse-sensor arrangement for Plate-C

Defect modeling and discrete surface strain measures are obtained from high-fidelity FEM analysis using an in-house FEA package. Next, the iFEM analysis is performed by considering sparse-sensor arrangement as depicted in Figure 22. For clarity, only iFEM displacement contours are discussed here to study the defect resolution potential of the iKP4 inverse-plate element.

The results for transverse displacement w_z and bending rotations $w_{,x}$ and $w_{,y}$ for iFEM sparse-sensor arrangement are shown in Figure 23. The transverse displacement contour does not show any displacement variations in the domain of defects; however, the contours for bending rotations depict bias in the defected domains of the plate. The displacement contour of bending rotation $w_{,y}$ significantly shows variation in the defected regions of the Plate-C.

Since the equivalent von Mises strain contour is sensitive to defective regions, the von Mises contour for Plate-C is essential for its defect resolution analysis. Using equation
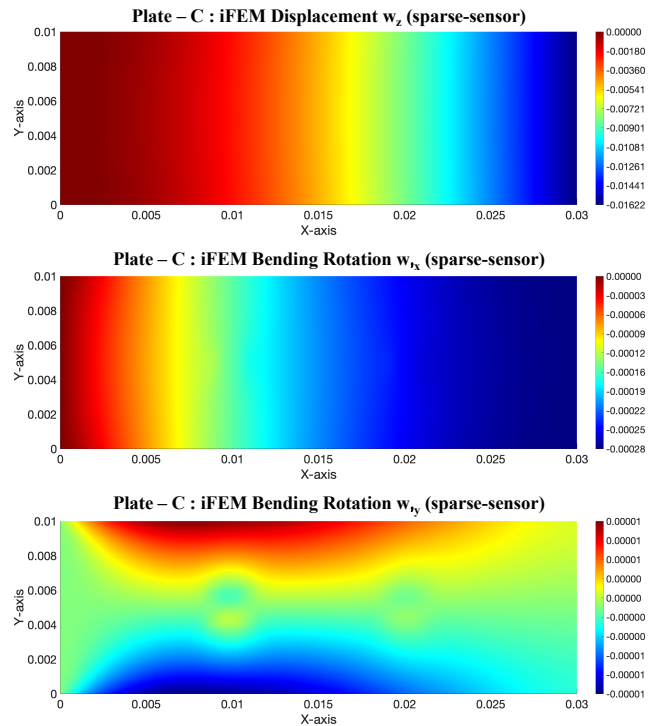

Figure 23: Transverse Loading : Transverse displacement w_z profile, bending rotation $w_{,x}$ profile, and bending rotation $w_{,y}$ profile
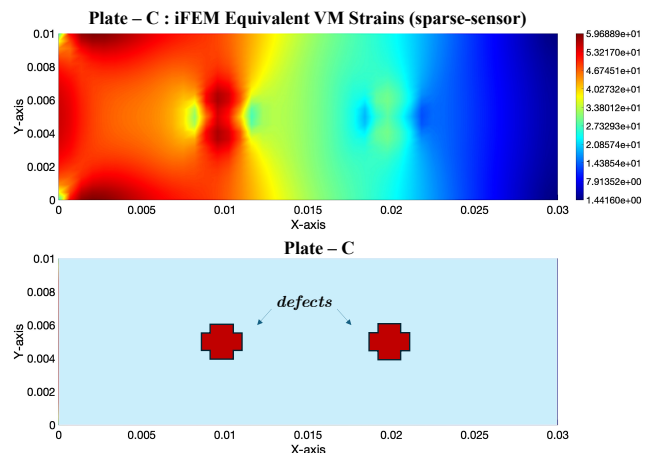

Figure 24: Transverse Loading : Equivalent von Mises strains contour for Plate-C

39, the von Mises strain plot generated during iFEM analysis of Plate-C under sparse-sensor arrangement is depicted in Figure 24. The plot shows significant variation in the exact domains of defects modeled via the stiffness degradation approach. It helps in precisely identifying and quantifying multiple subsurface defects present in Plate-C. The von Mises contours successfully resolve two defects located at the center of the plate at varying lengths.

A thorough defect resolution analysis ascertains the superior capability of the iKP4 inverse-plate element in the

identification and quantification of geometric discontinuities and subsurface defects appearing in thin plate structures when exposed to in-service general loading conditions. Therefore, the current iFEM formulation of the newly proposed inverse-plate element can be used in real-time SHM of various engineering structures, which can be modeled as thin plates.

5. Conclusion

In this study, a Kirchhoff-based two-dimensional four-node quadrilateral inverse-plate element (iKP4) is formulated using sub-parametric non-conforming cubic Hermite basis functions for thin plate structures. The proposed inverse element does not contain transverse shear terms in its formulation, which simplifies the governing equations and reduces potential sources of error. The error definition is inherently simpler, leading to potentially more accurate inverse analysis. Despite its higher continuity requirements, the element remains computationally efficient because neglecting transverse shear terms simplifies the overall iFEM formulation.

The inverse element is numerically validated against analytical and numerical reference solutions by considering in-plane, out-of-plane, and mixed general loading conditions considering homogeneous and composite materials. For all cases, iFEM analysis was undertaken for dense and sparse sensor arrangements to ascertain the capability of the proposed inverse-plate element in real-time shape-sensing applications. During validation, the iKP4 inverse-plate element demonstrated an accurate full-field reconstruction of deformation profiles under dense and sparse sensor arrangements. A detailed validation study concludes the superior capability of the iKP4 inverse-plate element for its real-time utilization in shape-sensing applications.

The proposed inverse-plate element is also analyzed for its defect resolution potential by validating it against minute geometric discontinuities and structural stiffness reduction because of latent subsurface defects under a sparse-sensor arrangement. A defect resolution study reveals the excellent capability of the iKP4 element in resolving and quantifying single or multiple defects of different natures. The iKP4 element, utilizing Kirchhoff plate kinematics, is an attractive inverse element for thin plate engineering structures and sandwich panels. Its accurate shape-sensing and defect-detection capabilities make it highly suitable for real-time shape-sensing and SHM applications.

A. Appendix

The explicit forms of bi-linear basis functions used for quadrilateral inverse-element are expressed here. These basis functions are utilised for geometric mapping and in-plane translational displacement variables as

$$N_1 = -\frac{(\eta - 1)(\xi - 1)}{4}$$
$$N_2 = -\frac{(\eta - 1)(\xi + 1)}{4}$$
$$N_3 = \frac{(\eta + 1)(\xi + 1)}{4}$$
$$N_4 = -\frac{(\eta + 1)(\xi - 1)}{4}$$

Similarly, the explicit forms of non-conforming cubic Hermite basis functions are outlined below for interpolating out-of-plane displacement variables as

$$M_1 = -\frac{(\eta - 1)(\xi - 1)(\eta^2 + \eta + \xi^2 + \xi - 2)}{8}$$
$$M_2 = \frac{(\eta - 1)(\xi + 1)(\eta^2 + \eta + \xi^2 - \xi - 2)}{8}$$
$$M_3 = \frac{(\eta + 1)(\xi + 1)(-\eta^2 + \eta - \xi^2 + \xi + 2)}{8}$$
$$M_4 = \frac{(\eta + 1)(\xi - 1)(\eta^2 - \eta + \xi^2 + \xi - 2)}{8}$$

$$M_{x1} = -\frac{(\eta - 1)(\xi - 1)^2(\xi + 1)}{8}$$
$$M_{x2} = -\frac{(\eta - 1)(\xi - 1)(\xi + 1)^2}{8}$$
$$M_{x3} = \frac{(\eta + 1)(\xi - 1)(\xi + 1)^2}{8}$$
$$M_{x4} = \frac{(\eta + 1)(\xi - 1)^2(\xi + 1)}{8}$$

$$M_{y1} = -\frac{(\eta - 1)^2(\eta + 1)(\xi - 1)}{8}$$
$$M_{y2} = \frac{(\eta - 1)^2(\eta + 1)(\xi + 1)}{8}$$
$$M_{y3} = \frac{(\eta - 1)(\eta + 1)^2(\xi + 1)}{8}$$
$$M_{y4} = -\frac{(\eta - 1)(\eta + 1)^2(\xi - 1)}{8}$$

References

[1] O. C. Zienkiewicz, R. L. Taylor, J. Z. Zhu, The finite element method: its basis and fundamentals, Elsevier, 2005.

[2] K. Tannhäuser, P. H. Serrao, S. Kozinov, A three-dimensional collocation finite element method for higher-order electromechanical coupling, Computers & Structures 291 (2024) 107219.

[3] S. Jiang, W. Deng, E. T. Ooi, L. Sun, C. Du, Data-driven algorithm based on the scaled boundary finite element method and deep learning for the identification of multiple cracks in massive structures, Computers & Structures 291 (2024) 107211.

[4] A. Di Matteo, Dynamic response of beams excited by moving oscillators: Approximate analytical solutions for general boundary conditions, Computers & Structures 280 (2023) 106989.

[5] E. Oterkus, E. Madenci, M. Nemeth, Stress analysis of composite cylindrical shells with an elliptical cutout, Journal of mechanics of materials and structures 2 (2007) 695–727.

[6] L. Nazarenko, R. Glüge, H. Altenbach, On variational principles in coupled strain-gradient elasticity, Mathematics and Mechanics of Solids 27 (2022) 2256–2274.

[7] D. De Meo, L. Russo, E. Oterkus, Modeling of the onset, propagation, and interaction of multiple cracks generated from corrosion pits by using peridynamics, Journal of Engineering Materials and Technology 139 (2017) 041001.

[8] Z. Yang, E. Oterkus, S. Oterkus, Peridynamic formulation for higher order functionally graded beams, Thin-Walled Structures 160 (2021) 107343.

[9] H. Guo, X. Zhuang, T. Rabczuk, A deep collocation method for the bending analysis of kirchhoff plate, arXiv preprint arXiv:2102.02617 (2021).

[10] E. Samaniego, C. Anitescu, S. Goswami, V. M. Nguyen-Thanh, H. Guo, K. Hamdia, X. Zhuang, T. Rabczuk, An energy approach to the solution of partial differential equations in computational mechanics via machine learning: Concepts, implementation and applications, Computer Methods in Applied Mechanics and Engineering 362 (2020) 112790.

[11] X. Zhuang, H. Guo, N. Alajlan, H. Zhu, T. Rabczuk, Deep autoencoder based energy method for the bending, vibration, and buckling analysis of kirchhoff plates with transfer learning, European Journal of Mechanics-A/Solids 87 (2021) 104225.

[12] W. L. Ko, W. L. Richards, V. T. Tran, Displacement theories for in-flight deformed shape predictions of aerospace structures, Technical Report, NASA, 2007.

[13] W. L. Ko, W. L. Richards, V. T. Fleischer, Applications of Ko displacement theory to the deformed shape predictions of the doubly-tapered Ikhana Wing, Technical Report, NASA, 2009.

[14] M. Gopinathan, G. A. Pajunen, P. Neelakanta, M. Arockaisamy, Recursive estimation of displacement and velocity in a cantilever beam using a measured set of distributed strain data, Journal of intelligent material systems and structures 6 (1995) 537–549.

[15] R. Glaser, V. Caccese, M. Shahinpoor, Shape monitoring of a beam structure from measured strain or curvature, Experimental mechanics 52 (2012) 591–606.

[16] M. Manola, V. Koumousis, Ultimate state of plane frame structures with piecewise linear yield conditions and multi-linear behavior: a reduced complementarity approach, Computers & Structures 130 (2014) 22–33.

[17] G. Foss, E. Haugse, Using modal test results to develop strain to displacement transformations, in: Proceedings of the 13th international modal analysis conference, volume 2460, 1995, p. 112.

[18] A. C. Pisoni, C. Santolini, D. E. Hauf, S. Dubowsky, Displacements in a vibrating body by strain gage measurements, in: Proceedings-SPIE the International Society for Optical Engineering, Citeseer, 1995, pp. 119–119.

[19] S. Shkarayev, R. Krashantisa, A. Tessler, An inverse interpolation method utilizing in-flight strain measurements for determining loads and structural response of aerospace vehicles, (No Title) (2004).

[20] M. Gherlone, P. Cerracchio, M. Mattone, Shape sensing methods: Review and experimental comparison on a wing-shaped plate, Progress in Aerospace Sciences 99 (2018) 14–26.

[21] J. S. Alexander Tessler, A variational principle for reconstruction of elastic deformations in shear deformable plates and shells, NASA (2003).

[22] A. Tessler, J. L. Spangler, A least-squares variational method for full-field reconstruction of elastic deformations in shear-deformable plates and shells, Computer Methods in Applied Mechanics and Engineering 194 (2005) 327–339.

[23] D. Yu, S. Wang, W. Li, Y. Yang, J. Hong, Shape sensing for thin-shell spaceborne antennas with adaptive isogeometric analysis and inverse finite element method, Thin-Walled Structures 192 (2023) 111154.

[24] S. Lee, M. Park, M.-H. Oh, P.-S. Lee, Virtual sensing for real-time strain field estimation and its verification on a laboratory-scale jacket structure under water waves, Computers & Structures 298 (2024) 107344.

[25] V. D. Fachinotti, A. E. Albanesi, J. M. M. Valle, Inverse finite element modeling of shells using the degenerate solid approach, Computers & Structures 157 (2015) 89–98.

[26] J. L. Spangler, A. Tessler, Inverse FEM for Full-Field Reconstruction of Elastic Deformations in Shear Deformable Plates and Shells, Technical Report, NASA, 2004.

[27] A. Kefal, E. Oterkus, Displacement and stress monitoring of a panamax containership using inverse finite element method, Ocean Engineering 119 (2016) 16–29.

[28] M. Abdollahzadeh, H. Q. Ali, M. Yildiz, A. Kefal, Experimental and numerical investigation on large deformation reconstruction of thin laminated composite structures using inverse finite element method, Thin-walled structures 178 (2022) 109485.

[29] A. Kefal, E. Oterkus, Isogeometric ifem analysis of thin shell structures, Sensors 20 (2020) 2685.

[30] F. Greco, L. Coox, F. Maurin, V. K. Balla, E. Deckers, W. Desmet, Reverse engineering of deep drawn components with an isogeometric framework, Computers & Structures 201 (2018) 15–25.

[31] J. Wang, L. Ren, R. You, T. Jiang, Z. Jia, G.-x. Wang, Experimental study of pipeline deformation monitoring using the inverse finite element method based on the ibeam3 element, Measurement 184 (2021) 109881.

[32] R. You, L. Ren, C. Yuan, G. Song, Two-dimensional deformation estimation of beam-like structures using inverse finite-element method: Theoretical study and experimental validation, Journal of Engineering Mechanics 147 (2021) 04021019.

[33] C. De Mooij, M. Martinez, R. Benedictus, ifem benchmark problems for solid elements, Smart Materials and Structures 28 (2019) 065003.

[34] A. Kefal, A. Tessler, E. Oterkus, An enhanced inverse finite element method for displacement and stress monitoring of multilayered composite and sandwich structures, Composite Structures 179 (2017) 514–540.

[35] A. Kefal, A. Tessler, E. Oterkus, An efficient inverse finite element method for shape and stress sensing of laminated composite and sandwich plates and shells, Technical Report, NASA, 2018.

[36] M. Li, E. Oterkus, S. Oterkus, A two-dimensional four-node quadrilateral inverse element for shape sensing and structural health monitoring, Mathematics and Mechanics of Solids (2023) 10812865231224384.

[37] D. Allman, A quadrilateral finite element including vertex rotations for plane elasticity analysis, International Journal for Numerical Methods in Engineering 26 (1988) 717–730.

[38] A. Ibrahimbegovic, R. L. Taylor, E. L. Wilson, A robust quadrilateral membrane finite element with drilling degrees of freedom, International Journal for Numerical Methods in Engineering 30 (1990) 445–457.

[39] S. Timoshenko, J. Goodier, Theory of elasticity, Inc. New York 1 (1951) 35–39.

[40] J. N. Reddy, An introduction to the finite element method, New York 27 (1993) 14.

[41] F. Siddiqui, Extended higher order theory for sandwich plates of arbitrary aspect ratio, Ph.D. thesis, PhD Thesis, School of Aerosapce Engineering, Georgia Institute of Technology, 2015.